



HAL
open science

Backward three-wave optical solitons

Carlos Montes, Antonio Picozzi, C. Durniak, M. Taki

► **To cite this version:**

Carlos Montes, Antonio Picozzi, C. Durniak, M. Taki. Backward three-wave optical solitons. The European Physical Journal. Special Topics, 2009, 173 (1), pp.167-191. <10.1140/epjst/e2009-01073-y>. <hal-00435147>

HAL Id: hal-00435147

<https://hal.science/hal-00435147v1>

Submitted on 25 Feb 2010

HAL is a multi-disciplinary open access archive for the deposit and dissemination of scientific research documents, whether they are published or not. The documents may come from teaching and research institutions in France or abroad, or from public or private research centers.

L'archive ouverte pluridisciplinaire HAL, est destinée au dépôt et à la diffusion de documents scientifiques de niveau recherche, publiés ou non, émanant des établissements d'enseignement et de recherche français ou étrangers, des laboratoires publics ou privés.



HAL Authorization

Backward Three-Wave Optical Solitons

Carlos Montes^{1,a}, Antonio Picozzi², Céline Durniak³, and Majid Taki³

¹ CNRS, Laboratoire de Physique de la Matière Condensée, Université de Nice - Sophia Antipolis, F-06108 Nice Cedex 2, France

² CNRS, Institut Carnot de Bourgogne, F-21078 Dijon Cedex, France

³ Laboratoire de Physique des Lasers, Atomes et Molécules, Université des Sciences et Technologies de Lille, F-59655 Villeneuve d'Ascq Cedex, France

Abstract. Backward symbiotic solitary waves in quadratic media with absorption losses are generated through the nonlinear non-degenerate three-wave interaction. We study these solitary waves in the particular case of a doubly backward quasi-phase matching configuration. The same mechanism responsible for nanosecond solitary wave morphogenesis in the c.w. pumped Brillouin-fiber-ring laser may act for picosecond pulse generation in a quadratic c.w. pumped optical parametric oscillator (OPO). The resonant condition is automatically satisfied in stimulated Brillouin backscattering when the fiber-ring laser contains a large number of longitudinal modes beneath the gain curve. However, in order to achieve quasi-phase matching between the three optical waves in the $\chi^{(2)}$ medium, a nonlinear susceptibility inversion grating of sub- μm period is required. Such a quadratic medium supports solitary waves that result from energy exchanges between dispersionless waves of different velocities. We show, by a stability analysis of the non-degenerate backward OPO in the QPM decay interaction between a c.w. pump and backward signal and idler waves that the inhomogeneous stationary solution exhibits a Hopf bifurcation with a single control parameter. Above OPO threshold, the nonlinear dynamics yields self-structuration of a backward symbiotic solitary wave, which is stable for a finite temporal walk-off (i.e. different group velocities) between signal and idler waves.

We also study the dynamics of singly backward mirrorless OPO's (BMOPO's) pumped by an incoherent field, in line with the recent experimental demonstration of this OPO configuration. We show that this system is characterized, as a general rule, by the generation of a highly coherent backward field, despite the high degree of incoherence of the pump field. This remarkable property finds its origin in two distinct phase-locking mechanisms that originate respectively in the convection and the dispersion properties of the fields. In both cases we show that the incoherence of the pump is transferred to the co-moving field, which thus allows the backward field to evolve towards a highly coherent state. We propose realistic experimental conditions that may be implemented with currently available technology and in which backward coherent wave generation from incoherent excitation may be observed and studied.

published in Eur. Phys. J. Special Topics **173**, 167-191 (2009)

^a e-mail: carlos.montes@unice.fr

1 Introduction

Resonance processes in nonlinear wave systems may give rise to solitary waves resulting from energy exchanges between dispersionless waves of different velocities. Three-wave resonant interaction in nonlinear optical systems [1], plasmas [2] [3] and gases [4] predict symbiotic three-wave solitary waves in analogy to self-induced transparency [5] [6]. The structure of them is determined by a balance between the energy exchanges rates and the velocity mismatch between the three interacting waves. The three-wave interaction problem has been the object of many theoretical studies and numerical simulations as we refered in Refs. [7] [8]. The non-conservative problem in the presence of a continuous pump has been integrated by the inverse scattering transform (IST) in the non-dissipative case [6], giving rise to backscattered solitons. Our interest has been to study this non-conservative problem in the presence of dissipation or cavity losses, because this kind of backward structuration has been experimentally obtained in stimulated Brillouin scattering of a c.w. pump wave into a backward red-shifted Stokes wave in long fiber-ring cavities. It has been shown in a Brillouin fiber-ring cavity that, spontaneous structuration of dissipative three-wave solitary waves takes place when the source is a c.w. pump [9–12]. The periodic round-trip interaction in a long lossy cavity may be associated to the non-conservative unlimited interaction [8] [11]. The nonlinear spacetime three-wave resonant model between the two optical waves and the dissipative material acoustic wave satisfactorily explains the generation and the dynamics of the backward-traveling solitary pulses in the fiber-ring cavities. Stability analysis of the inhomogeneous stationary Brillouin mirror solution in the c.w.-pumped cavity [10] exhibits a one-parameter Hopf bifurcation. Below a critical feedback, a time-dependent oscillatory regime occurs, and self-organization of a localized pulsed regime takes place. Experimental results and dynamical simulations confirm this scenario. A stable continuous family of super-luminous and sub-luminous backward-traveling dissipative solitary pulses is obtained through a single control parameter [11] [12]. A parallel analysis in an unbounded one-dimensional medium shows that the integrable three-wave super-luminous symmetrical soliton is unstable for small dissipation, and that it cascades to a turbulent multi-peak structure. The general non-symmetrical and non-integrable case is dependent only on the exponential slope of the wave front of the backscattered Stokes wave, thus providing the stable super- and sub-luminous dissipative solitary attractors [8]. An overview of the experimental results for a large set of input pump powers and Stokes feedback conditions shows a remarkable agreement with the numerical simulations of the three-wave coherent partial differential equations model [12]. In the following, we will not consider this topic here and refer the reader to a recent review article [13] where this kind of dissipative soliton has been discussed in details.

This review article is devoted to the resonant interaction of three optical waves (called pump, signal and idler) in a nonlinear quadratic material. The same mechanism, responsible for nanosecond solitary wave morphogenesis in the Brillouin-fiber-ring laser may act for picosecond backward pulse generation in a quasi-phase matched (QPM) optical parametric oscillator (OPO) [14–18]. The dissipative character will rise from the partial reinjection of one wave (in the singly resonant OPO), of two waves (in the doubly resonant OPO), or to the absorption losses in backward mirrorless OPO. The resonant condition for the wavevectors is automatically satisfied in stimulated Brillouin backscattering when the fiber ring laser contains a large number of longitudinal modes beneath the Brillouin gain curve. However, in order to achieve counter-streaming QPM matching between the three optical waves in the $\chi^{(2)}$ medium, a nonlinear susceptibility inversion grating of sub- μm period is required [20–23]. In the non-degenerate three-wave case of a backward quasi-phase matching configuration in the quadratic media where both signal and idler fields propagate backward with respect to the direction of the pump field, the first order quasi-phase-matching pitch is of order $\lambda_p/2n_p$ where n_p is the refractive index at the pump wavelength λ_p . This can be achieved for example by periodic poling techniques but up to now the polarization inverted grating of sub- μm period is still a technological challenge. Therefore higher-order Bragg condition have been suggested [22]. However, the interest of the first order configuration is that the solitary waves can be spontaneously generated from noise from a c.w. pump when the quadratic material is placed inside a singly resonant OPO (where

singly stands here for only one wave reinjection).

Parametric interaction of counter-propagating waves has the unique property of automatically establishing distributed feedback without external mirrors and thus realizing sources of coherent and tunable radiation. A recent experimental demonstration of such a mirrorless optical parametric oscillator (MOPO) has been performed in a 800 nm periodically poled KTiOPO_4 (PPKTP) configuration [24] with a pulse pump. The forward oscillator signal is essentially a wavelength-shifted replica of the pump spectrum, and the backward generated idler pulse has a bandwidth of two orders of magnitude narrower than that of the pump. This sub- μm periodic configuration where QPM is achieved with a pump and signal waves propagating in the forward direction and the idler wave in the backward direction opens the way for achieving the shorter periodicity required for a QPM configuration where both signal and idler backward propagate with respect to the pump wave [*cf.* figure 1(c)]. As we say, this doubly-backward configuration is of interest since the three-wave symbiotic solitary waves can be generated from noise in the presence of a c.w. pump when the quadratic material is placed inside an optical parametric oscillator [14–18]. However, with a c.w. pump the singly backward OPO yields stationarity for the backward wave. Nevertheless when the pump is a pulse, the demonstrated MOPO experimental configuration generates a coherent backward pulse in the absence of external feedback. Note that stationarity of the singly backward configuration in a c.w. pumped short length device is not contradictory with the theoretical existence of backward solitary solutions when the initial condition is localized [6]. Moreover, a coherent solitary structure can be sustained from a highly incoherent pump and a co-propagating wave [25]. This phenomenon relies on the advection between the interacting waves and leads to the formation of a novel type of three-wave parametric soliton composed of both coherent and incoherent fields. In section 5 we will consider this mechanism by proposing the generation of a coherent backward pulse from an incoherent pump pulse in three MOPO configurations, among which the first one refers to the experimental configuration demonstrated in Ref.[24]. We thus show that the MOPO system is characterized, as a general rule, by the generation of a highly coherent backward field, despite the high degree of incoherence of the pump field. In substance, the incoherence of the pump is shown to be transferred to the co-moving field, which thus allows the backward field to evolve towards a highly coherent state. We propose realistic experimental conditions that may be implemented with currently available technology and in which backward coherent wave generation from incoherent excitation may be observed and studied.

We have already shown, by both analytical and numerical treatments of the degenerate backward OPO in the QPM decay interaction between a c.w. pump and a backward signal wave, that the inhomogeneous stationary solutions are always unstable, whatever the cavity length and pump power values are above threshold of a singly resonant OPO. Starting from any initial condition, the nonlinear dynamics exhibits self-pulsing of the backward signal with unlimited amplification and compression. Above a critical steepening of the backward pulse, dispersion may saturate this singular behavior leading to self-modulated solitary structures [17] [19] as is shown in section 3.2.1.

In this paper we show, by a stability analysis of the non-degenerate backward OPO [18], that the previous particular behavior of unconditional temporal instability of the degenerate backward OPO is removed and that we now obtain a regular Hopf bifurcation like in the Brillouin fiber-ring laser [10]. We will consider self-structuration of three-wave solitary waves in such a backward OPO with absorption losses.

For a c.w. pumped OPO near degeneracy a unique control parameter L governs the dynamical behaviour; it is shown that at a critical interaction length L_{crit} the inhomogeneous stationary solution bifurcates towards a time-dependent oscillatory solution. This critical length is finite if and only if we take into account a finite group velocity delay between both backward propagating waves $\Delta v = |v_s - v_i| \neq 0$ (or temporal *walk-off*), where v_s and v_i are the signal and idler group velocities. Moreover, for longer interaction lengths the dynamics gives rise to the generation of the backward three-wave soliton, whose stability is also ensured by this finite

temporal walk-off Δv , without requiring additional saturation mechanisms like the dispersion effect. This *scenario* is confirmed by numerical simulations of the nonlinear dynamic equations, and an excellent agreement is obtained (near the degenerate configuration) for the value of L_{crit} evaluated from the stability analysis and that one obtained from the dynamical treatment.

The general fully non-degenerate configuration involves more complicated mathematics because a set of control parameters are required and we only show several dynamical behaviours resulting from the three-wave numerical model.

We will conclude this review by considering some dynamical behaviours of the backward mirrorless OPO pumped with an incoherent pulse, because up to now this configuration is the only one in which backward MOPO experiments have been performed.

The paper is organized as follows. In section 2 we recall the three-wave model governing the spatio-temporal evolution of the slowly varying envelopes of the pump and the backward signal and idler waves. We also recall the analytical solutions in the form of propagating dissipative solitary waves propagating backward with respect the cw-pump under a QPM three-wave interaction. In section 3 is presented the stability analysis of the nonlinear inhomogeneous stationary solutions of the non-degenerate backward OPO for finite temporal walk-off. Numerical dynamics of the self-structuration of symbiotic three-wave solitons leading to stable self-pulsing regimes is shown in section 4. Finally, the numerical dynamics of the pulsed MOPO under incoherent pump excitation is discussed in section 5.

2 Three-wave model and analytical solitary-wave solutions

The spatio-temporal evolution of the slowly varying envelopes of the three resonant counter-streaming interacting waves $A_j(x, t)$, for a non-degenerate OPO, is given by

$$\begin{aligned} (\partial_t + v_p \partial_x + \gamma_p + i\beta_p \partial_{tt}) A_p &= -\sigma_p A_s A_i \\ (\partial_t - v_s \partial_x + \gamma_s + i\beta_s \partial_{tt}) A_s &= \sigma_s A_p A_i^* \\ (\partial_t - v_i \partial_x + \gamma_i + i\beta_i \partial_{tt}) A_i &= \sigma_i A_p A_s^* \end{aligned} \quad (1)$$

where $A_p(\omega_p, k_p)$ stands for the c.w. pump wave, $A_s(\omega_s, k_s)$ for the backward signal wave, and $A_i(\omega_i, k_i)$ for the backward idler wave. The resonant conditions in one-dimensional configuration realize the energy conservation,

$$\omega_p = \omega_s + \omega_i, \quad (2)$$

and the momentum conservation,

$$k_p = -k_s - k_i + K_G, \quad (3)$$

where $K_G = 2\pi/\Lambda_{QPM}$ and Λ_{QPM} is the grating pitch for the backward quasi-phase matching. The group velocities v_j ($j = p, s, i$) as well as the attenuation coefficients γ_j are in general different for each wave. Equations (1) also hold for standard forward phase-matching configurations in which case all the signs of the velocities $v_{s,i}$ are positive. For the singly backward idler (or backward signal) configuration the momentum conservation (3) must be replaced by (17). These configurations are shown in figure 1(a)(b). The nonlinear coupling coefficients are $\sigma_j = 2\pi d_{eff} v_j / (\lambda_j n_j)$, where n_j is the refractive index at frequency ω_j , wavelength λ_j and d_{eff} is the effective nonlinear susceptibility. The chromatic dispersion is also taken into account in equations (1); this is necessary when the generated temporal structures are sufficiently narrow. The effects of group velocity dispersion (GVD) are represented by the second derivatives with respect to time, so that the dispersion parameters are given by $\beta_j = |v_j| k_j''$ where $k_j'' = (\partial^2 k / \partial \omega^2)_j$, k being the wave vector modulus, $k = n(\omega)\omega/c$.

2.1 Solitary Wave Solution

In the absence of dispersion ($\beta_j = 0$) equations (1) have been extensively studied in the literature. Their solitary wave solutions have been first derived in the absence of dissipation ($\gamma_j = 0$) [2, 6, 3]. In the context of stimulated scattering in nonlinear optics, the existence of dissipative solitary waves when one of the velocities $v_{s,i}$ is zero (*e.g.* $v_i = 0$) has also been shown [9, 26]. More recently, Craik *et al.* have proved, for the particular case of degenerate three-wave interaction, that solitary waves still exist in the presence of dissipation [27]. On the basis of these previous theoretical works, we have calculated from equations (1) a particular analytical solution of the dissipative symbiotic solitary waves of the non-degenerate parametric three-wave interaction. Looking for a solitary wave structure induced by energy transfer from the pump wave to the signal and idler pair, we have to assume zero loss for the pump ($\gamma_p = 0$). It is the only way to keep constant the energy transfer that compensates here for the signal and the idler losses, so as to generate stationary field structures. If γ_p was not zero, the pump wave would experience an exponential decay giving rise to a vanishing energy of the three-wave structure that prevents the formation of a stationary solitary wave state.

When $\gamma_p = 0$ it is easy to find by substitution the following solution to equations (1):

$$\begin{aligned} A_p &= \delta - \beta \tanh[\Gamma(x + Vt)] \\ A_s &= \eta \Gamma \operatorname{sech}[\Gamma(x + Vt)] \\ A_i &= \kappa \Gamma \operatorname{sech}[\Gamma(x + Vt)] \end{aligned} \quad (4)$$

where β is the only free parameter. All other parameters depend on the material properties and on β . One finds $\delta = [\gamma_s \gamma_i / \sigma_s \sigma_i]^{1/2}$, $\Gamma = \beta [\sigma_i \sigma_s / (V - v_s)(V - v_i)]^{1/2}$, $\eta = [(V + v_p)(V - v_i) / \sigma_i \sigma_p]^{1/2}$, $\kappa = [(V + v_p)(V - v_s) / \sigma_s \sigma_p]^{1/2}$, and $V = (v_s / \gamma_s - v_i / \gamma_i) / (1 / \gamma_s - 1 / \gamma_i)$. This last expression shows that the velocity V of the solitary wave is fixed by the material parameters, unlike in the nondissipative case where V is undetermined [2]. Let us point out that, in order to keep Γ real, the solitary wave must be either superluminal, $V > \max(v_s, v_i)$, or subluminal, $V < \min(v_s, v_i)$. Note that the superluminal velocity does not contradict by any means the special theory of relativity [9] even if the velocity V becomes infinite when the signal and idler waves undergo identical losses, $\gamma_s = \gamma_i$. This can be easily explained by remembering that the velocity of this type of symbiotic solitary wave is determined by the energy transfer rate, which depends on the shape of the envelope of each component. The infinite velocity is here simply due to the fact that the width of the solitary wave Γ^{-1} also becomes infinite for $\gamma_s = \gamma_i$. However, we shall see that this symmetrical solution is not the more general one and it is not an attractor solution for a large variety of parameter values. In section 4 we will present another self-similar structure for the near-degenerate backward interaction which does not present a divergence for $\gamma_s = \gamma_i$. The free wave parameter β fixes, in combination with the material parameters, the amplitude and the width of the solitary wave. According to the first equation of (4), β is determined by the initial pump amplitude $A_p = E_p(x = -\infty) = \beta + \delta$. In practice, this means that, for a given material, the solitary wave is completely determined by the pump intensity at the input face of the crystal. Note that if the losses are such that $\delta > \beta$ the solitary wave no longer exhibits a π -phase change [8], contrary to the nondissipative case [2].

Figure 2 shows a typical example of such a dissipative symbiotic solitary wave in a quasi-phase-matched backward three-wave interaction with $\lambda_p = 1 \mu\text{m}$, $\lambda_s = 1.5 \mu\text{m}$, $\lambda_i = 3 \mu\text{m}$, $A_{QPM} = 2\pi / K_G = 0.233 \mu\text{m}$, and with a pump field of amplitude $E_p = 0.25 \text{ MV/m}$ (*i.e.*, a pump intensity of $I_p = 10 \text{ kW/cm}^2$) propagating in a quadratic $\chi^{(2)}$ material. It is obtained with the following typical values of the parameters: $d_{eff} = 20 \text{ pm/V}$, $n_p = 2.162$, $n_s = 2.142$, $n_i = 2.098$, $v_p = 1.349 \times 10^8 \text{ m/s}$, $v_s = 1.371 \times 10^8 \text{ m/s}$, $v_i = 1.363 \times 10^8 \text{ m/s}$, and the loss coefficients $\alpha_s = 2\gamma_s / v_s = 0.23 \text{ m}^{-1}$ and $\alpha_i = 2\gamma_i / v_i = 11.5 \text{ m}^{-1}$. Note that these parameters lead to a pulse width of approximately 10 picoseconds. Therefore, with such pulse durations one can expect that the zero pump loss approximation ($\gamma_p = 0$) is valid in practice in the neighborhood of the solitary wave structure. Indeed, if the characteristic absorption length v_p / γ_p

is much larger than the pulse width Γ^{-1} , one can anticipate that the solitary wave undergoes adiabatic reshaping during propagation so as to adapt locally its profile to the exponentially decaying pump intensity.

3 Self-pulsing in a backward doubly resonant OPO

Let us point out that the self-structuration process requires backward interaction. The mechanism is similar to the Hopf bifurcation appearing in the counter-streaming Brillouin cavity [10]. Numerical simulations with the more usual forward phase-matching conditions only lead to the steady-state regime. This shows that the distributed feedback nature of the interaction plays a fundamental role in the pulse generation process. This observation is consistent with the conclusions of [23] where complex temporal pattern formation in backward-phase-matched second harmonic generation is studied and of our previous study of the degenerate backward OPO [19]. But in contrast to this last study, where no regular Hopf bifurcation was found by starting from the inhomogeneous stationary solutions, since above the threshold the perturbations always grow in time, we will show hereafter that in the non-degenerate backward OPO a regular Hopf bifurcation takes place. Below a critical parameter value, the inhomogeneous stationary solutions are stable, and above it the bifurcation leads to an also stable self-structured solitary wave. Our purpose in this section is to prove that in the non-degenerate configuration, the temporal walk-off, *i.e.* the group velocity delay between the signal and the idler waves ensures a regular Hopf bifurcation and leads to a stable self-structuration of the three-wave envelopes. For the sake of simplicity, we will focus here on the near-degenerate OPO regimes [18]. However, our results are more general and can be extended to the fully non-degenerate case in a similar way. We present here several dynamical behaviours.

We start from the dimensionless form of equations (1) which describe the non-degenerate backward OPO in the quasi-phase-matching decay interaction between a pump and counter-propagating signal and idler waves. We write them near the degeneracy with temporal walk-off on only one field. This is not a restriction but it is more convenient for mathematical calculations. The general case can be recovered by an appropriate change of variables. By introducing the following scalings:

$$u_p = \sqrt{1-d^2} \frac{A_p}{A_p^o}, \quad u_s = \sqrt{2(1-d)} \frac{A_s}{A_p^o}, \quad u_i = \sqrt{2(1+d)} \frac{A_i}{A_p^o}, \quad \tau = t/\tau_o, \quad \xi = \frac{x}{\Lambda}, \quad L = \frac{\ell}{\Lambda} \quad (5)$$

where A_p^o is the incident c.w. pump, $\tau_o = 2/(\sigma_p A_p^o)$ and $\Lambda = v_p \tau_o$ are the characteristic time and length and ℓ the cavity length, the dimensionless equations read:

$$\begin{aligned} \left(\frac{\partial}{\partial \tau} + \frac{\partial}{\partial \xi} + \mu_p + i\tilde{\beta}_p \frac{\partial^2}{\partial \tau^2} \right) u_p &= -u_s u_i \\ \left(\frac{\partial}{\partial \tau} - \frac{\partial}{\partial \xi} + \mu_s + i\tilde{\beta}_s \frac{\partial^2}{\partial \tau^2} \right) u_s &= u_p u_i^* \\ \left(\frac{\partial}{\partial \tau} - \alpha \frac{\partial}{\partial \xi} + \mu_i + i\tilde{\beta}_i \frac{\partial^2}{\partial \tau^2} \right) u_i &= u_p u_s^* \end{aligned} \quad (6)$$

where $\alpha = v_i/v_p$, $v_p = v_s$, $\mu_j = \gamma_j \tau_o$, and $\tilde{\beta}_j = \beta_j/\tau_o$. The full description of the OPO dynamics is obtained by taking into account, in addition to equations (6), the following boundary conditions for the doubly resonant cavity

$$u_s(\xi = L, \tau) = \rho_s u_s(\xi = 0, \tau), \quad u_i(\xi = L, \tau) = \rho_i u_i(\xi = 0, \tau), \quad u_p(\xi = 0, \tau) = \sqrt{1-d^2} \quad (7)$$

where $\rho_s = \sqrt{R_s}$ and $\rho_i = \sqrt{R_i}$ are the amplitude feedback coefficients. Note that we have introduced the new coefficients $1 \pm d$ by setting $d = (\sigma_s - \sigma_i)/\sigma_p$ and assuming a near-degenerate OPO configuration, *i.e.*, $\sigma_p \simeq \sigma_s + \sigma_i$.

3.1 Inhomogeneous stationary solutions

Without optical attenuation ($\mu_j = 0$) and in the absence of dispersion ($\beta_j = 0$), inhomogeneous stationary solutions $u_j^{st}(\xi)$, $j = \{p, s, i\}$ can be obtained from equations (6) by setting $\partial/\partial\tau = 0$. The assumption of zero loss parameters μ_j is not restrictive since the main dissipation in the OPO cavity comes from the finite feedback. In this case, the following conservation relations, also known as Manley-Rowe relations [28], hold

$$\begin{cases} |u_p^{st}|^2 - |u_s^{st}|^2 = \pm D_s^2 \\ |u_p^{st}|^2 - \alpha|u_i^{st}|^2 = \pm D_i^2 \end{cases} \quad (8)$$

For a doubly resonant OPO with the same feedback coefficient for the signal and idler fields, we have $D_s = D_i = D$. This leads to two types of stationary solutions : (i) $D^2 = |u_p^{st}|^2 - |u_s^{st}|^2 = |u_p^{st}|^2 - \alpha|u_i^{st}|^2$ and (ii) $D^2 = |u_s^{st}|^2 - |u_p^{st}|^2 = \alpha|u_i^{st}|^2 - |u_p^{st}|^2$.

In case (i), the following inhomogeneous stationary solutions are obtained

$$\begin{aligned} u_p^{st}(\xi) &= D \tanh^{-1} \left(\operatorname{arccotanh} \left(\frac{u_p^{st}(0)}{D} \right) + \frac{D\xi}{\sqrt{\alpha}} \right) \\ u_s^{st} &= \alpha u_i^{st} = \frac{D^2}{\sinh^2 \left(\operatorname{arccotanh} \left(\frac{u_p^{st}(0)}{D} \right) + \frac{D\xi}{\sqrt{\alpha}} \right)} \end{aligned} \quad (9)$$

while in case (ii),

$$u_p^{st}(\xi) = D \frac{u_p^{st}(0) - D \tan\left(\frac{D\xi}{\sqrt{\alpha}}\right)}{D + u_p^{st}(0) \tan\left(\frac{D\xi}{\sqrt{\alpha}}\right)} \quad u_s^{st}(\xi) = \sqrt{\alpha} u_i^{st}(\xi) = \frac{D \sqrt{1 + \frac{u_p^{st2}(0)}{D^2}}}{\cos\left(\frac{D\xi}{\sqrt{\alpha}}\right) + \frac{u_p^{st}(0)}{D} \sin\left(\frac{D\xi}{\sqrt{\alpha}}\right)} \quad (10)$$

where $u_p^{st}(0) = \sqrt{1 - d^2}$.

Let us consider the situation of short enough OPO cavities in order to avoid total depletion of the pump inside the cavity and to benefit from the monotonous gain of the singly pumped OPO; otherwise the signal and idler fields oscillate and may return part of this intensity to the pump. This is achieved by considering $D\xi \ll 1$. Thus, to the leading order, the inhomogeneous stationary solutions (10) are

$$u_p^{st}(\xi) \simeq \frac{u_p^{st}(0) - D^2 \frac{\xi}{\sqrt{\alpha}}}{1 + u_p(0) \frac{\xi}{\sqrt{\alpha}}} \quad \text{and} \quad u_s^{st}(\xi) = \sqrt{\alpha} u_i^{st}(\xi) \simeq \frac{D \sqrt{1 + \frac{u_p^{st2}(0)}{D^2}}}{1 + \frac{u_p^{st}(0)\xi}{\sqrt{\alpha}}} \quad (11)$$

Manley-Rowe relations (8) are used at $\xi = 0$ and $\xi = L$, together with the boundary conditions to determine the integration constants. A second order algebraic equation for D^2 is obtained

$$aD^4 + bD^2 - c = 0 \quad (12)$$

with

$$a = L^2/\alpha, \quad b = (1-R)(1 + \sqrt{1 - d^2}L/\sqrt{\alpha})^2 - 2\sqrt{1 - d^2}L/\sqrt{\alpha}, \quad c = (1 - d^2)[1 - R(1 + \sqrt{1 - d^2}L/\sqrt{\alpha})^2]$$

Once D is determined from the above expression, $u_s(0)$ and $u_i(0)$ can be calculated via the Manley-Rowe relations (8).

Note that we will only consider the case (ii) configuration; case (i) can be analysed in a similar way.

3.2 Stability analysis of the inhomogeneous stationary solutions

Following Ref.[18] let us first perform the linear stability analysis of the inhomogeneous stationary solutions (10) with respect to space-time-dependent perturbations in the absence of dispersion and optical attenuation, through

$$u_j(\xi, \tau) = u_j^{st}(\xi) + \delta u_j(\xi) e^{-i\omega\tau} \quad \text{where } j = p, s, i.$$

It is more convenient to introduce the new variables

$$\begin{aligned} P(\xi) &= u_p^{st}(\xi), \quad S(\xi) = u_s^{st}(\xi), \quad I(\xi) = S(\xi)/\sqrt{\alpha} = u_i^{st}(\xi), \\ Z(\xi) &= \delta u_p(\xi), \quad Y(\xi) = \delta u_s(\xi), \quad X(\xi) = \delta u_i(\xi), \end{aligned}$$

where $P(\xi)$, $S(\xi)$ and $I(\xi)$ stand for the inhomogeneous stationary solutions and $Z(\xi)$, $Y(\xi)$ and $X(\xi)$ for the space-time-dependent perturbations. Thus, the linearized problem associated with equations (6) reads

$$\begin{aligned} \frac{\partial Z}{\partial \xi} - i\omega Z &= -S\left(X + \frac{Y}{\sqrt{\alpha}}\right) \\ \frac{\partial Y}{\partial \xi} + i\omega Y &= -PX - \frac{SZ}{\sqrt{\alpha}} \\ \alpha \frac{\partial X}{\partial \xi} + i\omega X &= -PY - SZ \end{aligned} \tag{13}$$

The stability analysis is performed by solving the perturbative equations (13) with the inhomogeneous stationary solutions and by taking into account the boundary conditions for the cavity. This gives rise to an eigenvalue problem with a dispersion relation for the complex frequency ω . Following [10], [19] and [18] we will look for the stability of the cavity modes with frequency $\Re(\omega) \simeq 2\pi N/L$ [N integer and L being the dimensionless length ℓ/Λ defined in (5)] yielding to mode instability whenever $\Im(\omega) > 0$.

3.2.1 Absence of walk-off

Let us first recall the situation in the absence of temporal walk-off; the signal and idler waves have the same group velocity leading to $\alpha = 1$ in equations (13). We proceed as in the degenerate case [19] and we obtain the following dispersion relation

$$a_o + b_o \sin(\omega L) + c_o \cos(\omega L) = 0 \tag{14}$$

where the expressions of a_o , b_o and c_o are given in appendix A of Ref.[18]. It should be noted that equation (14) generalizes the dispersion relation in [19] for the degenerate case because it applies to the doubly-resonant backward OPO. The instability of each mode is determined from equation (14) when $\Im(\omega) > 0$. However, in the absence of walk-off, signal and idler perturbation equations are decoupled from the pump perturbation equation, and again it leads to unconditional temporal instability. We recall that this instability leads to the generation of a localized structure exhibiting unlimited amplification and compression [17] [19], whose collapse may be avoided by including the natural chromatic dispersion which is present in equations (1). We show in figure 3, for the degenerate case, the dynamical behaviour where the amplification of the solitary pulses is saturated by temporal modulation of the envelopes as shown in the upper inset graph of the figure. The lower inset graph shows the generated pulse structure before saturation, which takes place here at about 6000 round trips, when the pulse is so steep that dispersion breaks the unlimited amplification by modulating the pulse. The saturation dynamics has been obtained for a large set of dimensionless parameters (L , R) corresponding to different pump intensities, cavity lengths and signal feedback, and the saturation level depends on the dimensionless rate β_s/τ_0 . Here, dispersion corresponds to actual Type I (e-e)

polarization interaction in LiNbO₃ at 100°C, namely $\beta_p/v_p = 0.113 \text{ ps}^2/\text{m}$ for the pump at $\lambda_p = 0.775 \text{ }\mu\text{m}$, and $\beta_s/v_s = 0.893 \text{ ps}^2/\text{m}$ for the backward signal wave at $\lambda_s = 1.55 \text{ }\mu\text{m}$. The power requirement for backward OPO operation depends on the ability to achieve low-order QPM over centimeter lengths. For instance, for a first order QPM in LiNbO₃ the grating pitch is as small as $\Lambda_{QPM} = 2\pi/K_G = 0.179 \text{ }\mu\text{m}$. For a c.w. pump field $E_p = 0.725 \text{ MV/m}$ (*i.e.*, a pump intensity of $I_p = 100 \text{ kW/cm}^2$) propagating in the quadratic $\chi^{(2)}$ material with the following values of the parameters: $d = 20 \text{ pm/V}$, $d_{eff} = 2d/\pi$, $n_p = 2.179$, $n_s = 2.141$, $v_p = 1.323 \times 10^8 \text{ m/s}$, $v_s = 1.371 \times 10^8 \text{ m/s}$, $\gamma_p = 4.6 \times 10^8 \text{ s}^{-1}$, and $\gamma_s = 3.1 \times 10^8 \text{ s}^{-1}$; the nonlinear characteristic time yields $\tau_0 = (\sigma_p A_p/2)^{-1} \simeq 0.28 \text{ ns}$. For $L = \ell/\Lambda = 1$ the cavity length ℓ is given by the nonlinear characteristic length $\Lambda = v_p \tau_0 = 3.7 \text{ cm}$. The solitary pulses are compressed until 7.5 ps before dispersion begins the saturation process. The dynamic solitary structure being deeply modulated by the presence of the phase defects, the central peak has about 5 ps width, while the whole pulse spreads over some tens of picoseconds.

Since the required grating pitch for first order QPM is extremely small, we must increase the c.w. pump intensity when using higher order gratings in order to get an actual experimental configuration. Reference [21] gives a table with the threshold pump intensities and domain periods for the degenerate backward OPO in four periodic domain structures (KTP, LiNbO₃, GaAs/AlAs). Recently [29], it has been reported an experiment of first order QPM blue light generation at 412.66 nm, in a 20 mm long surface-poled Ti-indiffused channel waveguide in LiNbO₃ with c.w. pumping, using periodic domain structures as short as 1 μm . The authors have announced generation of 3.46 mW blue light for 70 mW of fundamental power. Based on such recent progresses in the poling technology of LiNbO₃ one can likely hope to experimentally realize the backward OPO with the allowed pump power for so short grating pitch. We will see in section 5 that a periodic domain of 800 nm has been obtained in a bulk PPKTP configuration to achieve for the first time the pulsed mirrorless OPO. For example, if $\Lambda_{QPM} = 0.5 \text{ }\mu\text{m}$ we may only use a c.w. pump power ten times higher (*i.e.* $I_{p,0} = 1 \text{ MW/cm}^2$) for the same cavity length $\ell = 3.7 \text{ cm}$, same characteristic time $\tau_0 \simeq 0.28 \text{ ns}$, and same low finesse $\rho_s = \sqrt{R} = 0.46$ as that given in the previous example. If we consider a pulse pump of FWHM of $\Delta t = 28 \text{ ns}$ instead of a c.w. beam we can even reach $I_{p,0} = 100 \text{ MW/cm}^2$ without optical damage [30] (yielding $\tau_0 = 28 \text{ ps}$ and $\Lambda = 0.37 \text{ cm}$).

3.2.2 Finite temporal walk-off

When taking into account a finite temporal walk-off $\alpha \neq 1$, equations (13) are more complicated as the dynamics of the pump wave and the signal-idler pair is no longer decoupled. For the sake of simplicity let us consider $D = 0$, so that $P = S = \sqrt{\alpha}I = 1/(1/\sqrt{1-d^2} + \xi/\sqrt{\alpha})$. Note that $D = 0$ requires that $c = 0$ in equation (12). Since $d \ll 1$, it is the second factor in the same expression of c which vanishes leading to the relation $R = 1/(1 + \sqrt{(1-d^2)L/\sqrt{\alpha}})^2$. The first-order perturbed system becomes

$$\frac{d}{d\xi} \begin{pmatrix} Z \\ Y \\ X \end{pmatrix} = \begin{pmatrix} i\omega & -I & -S \\ -I & -i\omega & -P \\ -S/\alpha & -P/\alpha & -i\omega/\alpha \end{pmatrix} \begin{pmatrix} Z \\ Y \\ X \end{pmatrix}$$

This system of equations is numerically solved. Since the group velocity delay (temporal walk-off) of the signal and idler pair is small, we set $\alpha = v_i/v_p \simeq 1 + \epsilon$. We expand the solutions up to the second order in the small parameter ϵ . The second order is necessary to match the critical parameter value obtained at the Hopf bifurcation point by the numerical integration of the normalized governing equations (6); the first order in ϵ being insufficient to characterize the bifurcation point.

Through the boundary conditions, we obtain the dispersion relation:

$$\begin{aligned} & \omega^3 y_o^2 y_L + \left[-\omega^3 y_o^2 y_L - i\omega^2 y_o L + \omega L \right] \cos(\omega L) + \left[i\omega^3 y_o^2 y_L + i\omega y_o - \omega^2 y_o L - 1 \right] \sin(\omega L) \\ & - \frac{i\epsilon}{8y_L(y_o\rho_o - y_L e^{-i\omega L})} \left\{ A_o e^{-2i\omega L} + B_o e^{-i\omega L} + C_o e^{i\omega L} + D_o \right\} \\ & - \frac{i\epsilon^2}{24y_L^2(y_o\rho_o - y_L e^{-i\omega L})} \left\{ A_1 e^{-2i\omega L} + B_1 e^{-i\omega L} + C_1 e^{i\omega L} + D_1 \right\} = 0 \end{aligned} \quad (15)$$

with $y_o = 1/\sqrt{1-d^2}$, $y_L = y_o + L$, $\rho_o = y_o/y_L$ is the amplitude feedback coefficient and L stands for the dimensionless length ℓ/Λ . The expressions of the different coefficients A_o, A_1, B_o, B_1, C_o , and C_1 , which are functions of $\omega = \omega_r + i\omega_i$, y_L , and y_o are given in appendix B of Ref.[18]. First we recover, as it should be, the dispersion relation (14) when $\epsilon = 0$ and $D = 0$. However, the non-degenerate backward OPO dispersion relation (15) shows that, in contrast to the degenerate case, there exist a stability domain of the inhomogeneous stationary solutions above threshold. Moreover, these solutions undergo a Hopf bifurcation, even near the degenerate configuration, for a critical length of the cavity. Figure 4 shows a typical example of a regular Hopf bifurcation with the parameters set to $d = 0.05$ and $\epsilon = 1/128$. We have plotted $\Im(\omega)$ from equation (15) against the propagation length L near the first cavity mode ($\Re(\omega) \simeq 2\pi/L$). As can be seen from the figure, Hopf bifurcation occurs at $L_{crit} \simeq 0.39$. For $L \leq L_{crit}$ the inhomogeneous stationary solutions are stable (see figure 5) whereas if $L > L_{crit}$ the perturbations are amplified generating a new oscillatory localized structure (see figures 6 and 7).

4 Nonlinear dynamics of the doubly resonant backward OPO

In the previous section we have carried out the stability analysis of the inhomogeneous stationary solutions of the doubly resonant backward OPO near the degenerate configuration. This behavior may be generalized to the fully non-degenerate backward OPO provided that a finite temporal walk-off between the counter-propagating signal and idler waves is present. In this section we proceed as follows:

- (i) we numerically check the previous analytical result in the near-degenerate OPO regime for $D = 0$;
- (ii) we show that a dynamically critical bifurcation for $D \neq 0$ can be obtained with the same feedback parameter values ($\rho_s = \rho_i$) for both signal and idler waves;
- (iii) we numerically investigate the self-pulsing regime for the doubly resonant backward OPO with different feedback parameter values ($\rho_s \neq \rho_i$) including perturbative dispersion.

To this end we have numerically integrated equations (6) with the boundary conditions (7). In order to better compare the dynamical behavior with the analytical one, we first neglect dispersion ($\tilde{\beta}_j = 0$, $j = p, s, i$) which is only a perturbative effect in the non-degenerate case, but we include a small dissipation ($\mu_j = 10^{-2}$). In order to dynamically investigate the near-degenerate OPO regime for $D = 0$, we start from the approximate stationary solutions (11) with a group velocity difference (temporal walk-off) $|v_s - v_i|/v_p = 1/128$. In the near-degenerate OPO case, the feedback $R = |\rho_s|^2 = |\rho_i|^2$ is related to the dimensionless length L through the relation $u_p^2(L) - Ru_s^2(L) = D^2$, which is now simply reduced to $R = [1 + L\sqrt{(1-d^2)/\alpha}]^{-2}$. Therefore, we may investigate the near-degenerate OPO dynamics by varying the control parameter L from 0.25 to 0.5. As expected from the stability analysis, we now find a regular Hopf bifurcation of the stationary state towards a time-dependent oscillatory state for a critical length L_{crit} between 0.35 and 0.4, in contrast to the full degenerate case [19] or to the near-degenerate case $D = 0$ in the absence of temporal walk-off [cf. section 3.2.1], where no Hopf bifurcation exists. The stationary spatial profiles are shown in figure 5 after 16384 round trips for $L = 0.35$. This stationary state bifurcates towards a stable oscillatory regime as illustrated in Fig. 6 for $L = 0.4$. For a larger length L (and correspondingly smaller feedback R) we obtain pulsed regimes as that shown in figure 7 whose stability is ensured by the finite temporal

walk-off too, without taking into account any dispersion effect (*cf.* 8).

The dynamical equations (6) allow us to look further for $D \neq 0$, while the control parameter L (since R is only a function of K for $D = 0$) splits now into two control parameters L and R related through $u_p^2(L) - Ru_s^2(L) = D^2$. For $L = 0.25$ we obtain the Hopf bifurcation between $\sqrt{R} = 0.80$ and 0.81 , while for $L = 0.5$ it happens between $\sqrt{R} = 0.81$ and 0.82 , the pulsed regimes corresponding to lower feedback favors the localization of the structure [11]. For a typical pulsed regime at $L = 0.5$ and $\sqrt{R} = 0.81$, we show in figure 8 the saturation of the pulse maximum amplitude with time when starting from the stationary state, and in figure 9 a pair of two consecutive pulses in the asymptotic stable state (the width δt is measured in $t_r = \ell/v_s$ units). As can be seen from figure 10 the solitary structure is now composed of two embedded pulses of nearly identical amplitudes moving together, the constant spatial shift between them corresponds to the temporal walk-off (or different group velocities). The trapping between the signal and idler envelopes yields the new self-similar structure moving at a characteristic velocity, which is composed of the couple of embedded pulses maintaining constant spatial shift between them in spite of the different velocities of both waves.

Let us consider a physical application. In comparison to the type I (e-e) polarization interaction in LiNbO₃ proposed in section 3.2.1 and Ref. [19] for the full-degenerate case, we may now consider a type II (e-o-e) polarization interaction in order to move away from the degeneracy and to obtain a finite group velocity delay (or temporal walk-off) between the signal and the idler waves. For the same quadratic $\chi^{(2)}$ material, same pump wave (e-polarized) at $\lambda_p = 0.775 \mu\text{m}$, the same idler wave (e-polarized) at $\lambda_i = 1.55 \mu\text{m}$, but now a signal wave (o-polarized) at $\lambda_s = 1.55 \mu\text{m}$ having a different refractive index, the group velocity dispersion ensures a finite temporal walk-off between both backward waves. For a first order QPM in LiNbO₃ the grating pitch is as small as $\Lambda_{QPM} = 2\pi/K_G = 0.177 \mu\text{m}$. For a c.w. pump field $E_p = 0.725 \text{ MV/m}$ (*i.e.*, a pump intensity of $I_p = 100 \text{ kW/cm}^2$) propagating in this configuration we have the following values of the parameters [30]: $d_{eff} = 6 \text{ pm/V}$, $n_p = 2.181$, $n_s = 2.212$, $n_i = 2.140$, $v_p = 1.317 \times 10^8 \text{ m/s}$, $v_s = 1.323 \times 10^8 \text{ m/s}$, $v_i = 1.372 \times 10^8 \text{ m/s}$, $\gamma_p = 4.6 \times 10^8 \text{ s}^{-1}$, and $\gamma_s = \gamma_i = 3.1 \times 10^8 \text{ s}^{-1}$. The nonlinear characteristic time yields $\tau_0 = (\sigma_p A_p/2)^{-1} \simeq 0.94 \text{ ns}$, and the nonlinear characteristic length $\Lambda = v_p \tau_0 = 12 \text{ cm}$. We have taken cavity lengths running from 3 cm ($L = 0.25$) to 6 cm ($L = 0.5$) and we obtain a temporal width of the solitary pulses of the order of 100 ps.

Critical bifurcation parameters for doubly resonant backward OPOs with different nonlinear coupling coefficients σ_j and different feedback parameter values ($\rho_s \neq \rho_i$) may be obtained through the general dynamical equations (1) with boundary conditions (7). Figure 11 displays a typical self-pulsing regime for $\sigma_s/\sigma_p = 0.675$, $\sigma_i/\sigma_p = 0.350$, $L = 1$, $\beta_j = 10^{-6}$, $j = \{p, s, i\}$, $\rho_s = 0.9$ and $\rho_i = 0.6$. As can be seen from this figure the predicted stability of the self-pulsing regime is not affected by the presence of chromatic dispersion.

5 Backward coherent pulse from incoherently pumped mirrorless OPO

The numerical dynamics of a c.w. pumped singly backward OPO, experimentally adapted for an integrated cavity or IOPO (see for exemple [31–34]), either for counter-propagating signal or for counter-propagating idler does not generate backward solitary structures. Even for high OPO finesse the laser output is always stationary. Note that this does not contradict the existence of backward solitons in singly counter-propagating configurations if the backward wave is initially localized [2] [3] [25]. It simply means that such solitary waves cannot be spontaneously generated from quantum noise and a c.w. pump. Nevertheless, we shall see in this section that the singly backward OPO configuration is interesting from another point of view, namely the generation of a coherent backward pulse from an incoherent pump pulse. In this section we will show that recent experimental demonstration of a backward mirrorless optical parametric oscillator (BMOPO) with a pump pulse in the quasi-phase-matched (QPM) periodic polarized KTiOPO₄ crystal [24] opens the way for achieving ultra-coherent output through two distinct

phase-locking mechanisms, which originate respectively in the convection and the dispersion properties of the three interacting waves.

(i) The incoherence of the pump is absorbed by the co-propagating wave moving at the same group velocity of the pump through the *convection-induced phase-locking mechanism* [25] [35] [36] [37].

(ii) The incoherence of the pump is absorbed by the co-propagating wave having the *same group-velocity dispersion* as the pump [38].

In both cases the incoherence of the pump is transferred to the co-moving field, which permits the backward field to reach a highly coherent state.

The first mechanism (i) requires a matched group-velocity for the pump and the co-propagating idler wave, which may be achieved in a type I OPO for a pump at $1.060 \mu\text{m}$, a counterpropagating signal at $1.534 \mu\text{m}$ and an idler at $3.422 \mu\text{m}$. We will show that the degree of coherence of the backward signal field turns to be more than four orders of magnitude greater than that of the incoherent pump, with approximately the same pump power and crystal length as in the experiment [24].

The alternative phase-locking mechanism (ii) takes place for matched group-velocity dispersion coefficients of the co-propagating waves. This may occur using almost the same wavelength triplet as in [24] and a QPM grating period slightly longer, but using a type II configuration of the KTP crystal. The (y-polarized) pump and the co-propagating (z-polarized) signal have the same group-velocity dispersion and the numerics shows that a compensation of the group-velocity difference may occur. In this case the coherence of the idler field is shown to increase more than three orders of magnitude.

Parametric interaction of counterpropagating optical waves has the unique property of automatically establishing distributed feedback without external cavity mirrors; the mirrorless optical parametric oscillator has been the object of several studies [28] [39] [21] [40]. The recent BMOPO experiment exhibits useful spectral properties and has been performed in a configuration of type I at $\lambda_p = 0.8214 \mu\text{m}$, $\lambda_s = 1.1397 \mu\text{m}$ and $\lambda_i = 2.9408 \mu\text{m}$ with a grating period of $\Lambda_{QPM} = 0.8 \mu\text{m}$. This singly backward configuration overcomes the extremely low sub- μm grating periodicity required for the doubly backward OPO (*cf.* sections 3 and 4).

We have already proposed two experimental configurations in type II singly resonant KTP IOPO's [36] and in a type I $\{eee\}$ singly resonant Ti:LiNbO_3 IOPO [37], to show the mechanism (i) in standard high finesse forward propagating OPO's fed with a c.w. pump. We will show in this section the feasibility of coherent backward generation from an incoherent pump pulse in different mirrorless (without external feedback) BMOPO configurations fed with a pulse pump.

5.1 MOPO threshold and dynamical equations

A theoretical model yields an estimate of the MOPO threshold for counterpropagating plane waves [21], which is reached when the spatial gain exceeds $\pi/2$:

$$I_{pth} = \frac{\varepsilon_0 c n_p n_s n_i \lambda_s \lambda_i}{2 \ell^2 d_{eff}^2} \quad (16)$$

where ε_0 is the permittivity of free space, ℓ the interaction length, d_{eff} the effective quadratic nonlinear coefficient, and $n_{s,i}$, $\lambda_{s,i}$ the respective signal and idler refractive index and wavelength. For example, for a PPKTP crystal of $d_{eff} = 8 \text{ pm/V}$ we have:

$$\ell = 1 \text{ cm} \quad \implies \quad I_{pth} = 0.64 \text{ GW/cm}^2 ; \quad \ell = 5 \text{ mm} \quad \implies \quad I_{pth} = 2.56 \text{ GW/cm}^2.$$

This threshold is somewhat higher for an incoherent pump when condition (i) is not fulfilled, but it turns to be the same for strictly a random phase fluctuating pump [37]. The momentum mismatch for the optical parametric generation process for the singly backward QPM configuration yields now

$$k_p = \pm k_s \mp k_i + K_G, \quad (17)$$

where $(+k_s, -k_i)$ stands for backward idler propagation and $(-k_s, +k_i)$ for backward signal propagation [*cf.* figure 1 respectively (a) and (b)], which a resulting larger QPM grating period as that of the doubly backward OPO configuration. The schematic vector diagram and periodically domain-inverted ferroelectric crystal of the counterpropagating interaction are shown in figure 1, and equations (1) become:

$$\begin{aligned} (\partial_t + v_p \partial_x + \gamma_p + i\beta_p \partial_{tt}) A_p &= -\sigma_p A_s A_i \\ (\partial_t \pm v_s \partial_x + \gamma_s + i\beta_s \partial_{tt}) A_s &= \sigma_s A_p A_i^* \\ (\partial_t \mp v_i \partial_x + \gamma_i + i\beta_i \partial_{tt}) A_i &= \sigma_i A_p A_s^*. \end{aligned} \quad (18)$$

with respectively $(+v_s, -v_i)$ for the backward idler propagation and $(-v_s, +v_i)$ for the backward signal propagation.

5.2 BMOPO I actual experimental realization

The QPM three-wave resonant coupling in the experimental achieved BMOPO of type I in a bulk PPKTP crystal correspond to the following parameters [24]:

$$\begin{aligned} \lambda_p &= 0.8214 \mu\text{m}; n_p = 1.8434; v_p/c = 0.5240; \beta_p = 0.2736 \text{ ps}^2/\text{m} \\ \lambda_s &= 1.1397 \mu\text{m}; n_s = 1.8270; v_s/c = 0.5357; \beta_s = 0.1613 \text{ ps}^2/\text{m} \\ \lambda_i &= 2.9408 \mu\text{m}; n_i = 1.7846; v_i/c = 0.5373; \beta_i = -0.3269 \text{ ps}^2/\text{m} \end{aligned}$$

where

$$\begin{aligned} A_{QPM} &= \left[\frac{n_p}{\lambda_p} - \frac{n_s}{\lambda_s} + \frac{n_i}{\lambda_i} \right]^{-1} = 0.8012 \mu\text{m} \\ \Delta v/v_s &= |v_p - v_s|/v_s = 0.02184 \simeq 1/46, \end{aligned}$$

and the counter-propagation interaction corresponds to figure 1(a). The experimental point of operation is plotted on the group-velocity dispersion curves shown in figure 12.

Let us show the dynamical behaviours for a BMOPO of 7 mm length pumped with a 60 ps pulse duration of $I_p = 1.6 \text{ GW}/\text{cm}^2$ maximum intensity and increasing incoherence characterized by a frequency bandwidth $\Delta\nu_p$ running from 220 GHz to 1.5 THz. Figures 13 to 16 show the respective outgoing field amplitudes versus time and their corresponding power spectra. We see that despite the fact that neither condition (i) nor condition (ii) are strictly satisfied, the backward configuration leads to the generation of a highly coherent idler field. We will see in the next section that this effect can be improved by satisfying condition (ii) in a type II configuration. This configuration is characterized by a smaller nonlinear coefficient but a larger QPM grating pitch. We will consider in the last section the case where condition (i) is fulfilled.

5.3 BMOPO II for exact dispersion mismatch

In order to improve the coherence transfer we will first use mechanism (ii) which has been described in [38]. However, to obtain a good dispersion mismatch between the co-propagating pump and signal waves ($\beta_p = \beta_s$) we propose the following type II configuration in PPKTP:

$$\begin{aligned} \lambda_p &= 0.821 \mu\text{m}; n_p = 1.7555; v_p/c = 0.5550; \beta_p = 0.1921 \text{ ps}^2/\text{m} \\ \lambda_s &= 1.028 \mu\text{m}; n_s = 1.8314; v_s/c = 0.5329; \beta_s = 0.1921 \text{ ps}^2/\text{m} \\ \lambda_i &= 4.077 \mu\text{m}; n_s = 1.6821; v_i/c = 0.5556; \beta_s = -0.8616 \text{ ps}^2/\text{m} \end{aligned}$$

where

$$\Lambda_{QPM} = \left[\frac{n_p}{\lambda_p} - \frac{n_s}{\lambda_s} + \frac{n_i}{\lambda_i} \right]^{-1} = 1.30 \mu\text{m}$$

$$\frac{\Delta v}{v_p} = \frac{|v_p - v_s|}{v_p} = 0.04 \simeq 1/25.$$

This backward interaction is also illustrated schematically in figure 1(a). Now the y-polarized pump and the co-propagating z-polarized signal have the same group-velocity dispersion and the dynamics will prove compensation of the group-velocity difference between these waves. The proposed point of operation is plotted on the group-velocity dispersion curves shown in figure 17. We perform the numerical dynamics from equations (18), with $(+v_s, -v_i)$, taking a highly incoherent ns pump pulse duration of 25 THz bandwidth and a higher maximum pump intensity $I_p = 2.8 \text{ GW/cm}^2$ in order to compensate the lower effective nonlinear coefficient, namely $d_{eff} = 6 \text{ pm/V}$. Figures 18 and 19 reveal a remarkable coherence transfer from the pump to the signal, so that the backward idler field turns out to be highly coherent.

As we can see, the signal spectrum exhibits a significant frequency shift $\Delta\nu_{shift}$. The frequency shift is such that the signal group-velocity approximately matches the pump group-velocity, namely $\Delta v/v_s \simeq 2\pi\Delta\nu_{shift}v_s\beta_s$, as expected from [38]. However, because of the finite pulse duration of the interaction we do not reach an asymptotic behavior. Nevertheless, let us underline the gain of coherence in the idler field, which exceeds three orders of magnitudes.

5.4 BMOPO III for exact group velocity mismatch

Let us now consider the situation where the two co-propagating waves have the same group velocity which relies on the convection-induced phase-locking mechanism (**i.**), already proposed for c.w. pumped OPO's [36] [37]. In order to benefit of a type I configuration in PPKTP, the singly backward wave may be now the signal, the co-propagating pump and idler waves satisfying $v_p = v_i$; this interaction corresponds to the counter-propagation schema shown in figure 1(b). The proposed point of operation is plotted on the group-velocity dispersion curves shown in figure 20 and the type I configuration may be the following:

$$\lambda_p = 1.060\mu\text{m}; n_p = 1.8300; v_p/c = 0.5338; \beta_p = 0.182 \text{ ps}^2/\text{m}$$

$$\lambda_s = 1.534\mu\text{m}; n_s = 1.8163; v_s/c = 0.5401; \beta_s = 0.076 \text{ ps}^2/\text{m}$$

$$\lambda_i = 3.429\mu\text{m}; n_i = 1.7709; v_i/c = 0.5338; \beta_i = -0.579 \text{ ps}^2/\text{m}$$

where

$$\Lambda_{QPM} = \left[\frac{n_p}{\lambda_p} + \frac{n_s}{\lambda_s} - \frac{n_i}{\lambda_i} \right]^{-1} = 0.4177 \mu\text{m}$$

$$\frac{\Delta v}{v_p} = \frac{|v_p - v_i|}{v_p} = 0$$

We perform the numerical dynamics from equations (18) with $(-v_s, +v_i)$ taking a similar highly incoherent ns pump pulse duration of 25 THz bandwidth. However, we consider maximum pump intensity of only $I_p = 1.6 \text{ GW/cm}^2$, since we take advantage of the greater effective nonlinear coefficient, namely $d_{eff} = 8 \text{ pm/V}$. The experimental constraint turns to be here the short QPM grating pitch Λ_{QPM} required for the first order interaction. Figures 21 and 22 show that, as expected, the pump transfers its noise to the idler field, which thus leads to the generation of a highly coherent backward signal pulse. As remarkably shown in the figures, the gain of coherence now exceeds four orders of magnitude.

5.5 Convection-induced phase-locking mechanism

The coherent properties of the parametric three-wave interaction driven from an incoherent pump has been the object of an analytical study where the autocorrelation functions are mathematically evaluated in the presence of dispersion [35] and the convection-induced phase-locking mechanism has been proposed for forward OPO's configurations [36] [37]. Let us present here some simple analytical arguments enlighting the mechanism **(i)** from equations (18) for the singly backward signal configuration [case (b) of figure 1], Let us assume the dispersioless case ($\beta_j = 0$), $\sigma_s = \sigma_i = \sigma_p/2 = \sigma$, and the linear undepleted pump limit with $\gamma_p = 0$. The incoherent pump may be modeled by a stationary single-variable stochastic function $A_p(z)$ of autocorrelation function

$$\frac{\langle A_p(z - z')A_p^*(z') \rangle}{|A_p(0)|^2} = \exp\left(-\frac{|z|}{\lambda_c}\right)$$

with a coherence length λ_c in the frame traveling at its group velocity v_p ,

$$z = x - v_p t,$$

the correlation time being $\tau_c \simeq 1/\pi\Delta\nu_p$, where $\Delta\nu_p$ is the incoherent (broad)-bandwidth of the pump spectrum. The role of convection in the coherence of the generated waves A_s and A_i may be analyzed by integrating the third equation (18) along the characteristic of the idler wave. Then, the second equation (18) yields

$$DA_s = \sigma^2 \int_0^t e^{-\gamma_i(t-t')} A_p(z) A_p^*(z') A_s(x', t') dt'$$

where

$$D = \partial/\partial t - v_s \partial/\partial x + \gamma_s$$

$$z' = z - (v_i - v_p)(t - t') ; \quad x' = x - v_i(t - t')$$

If $v_i = v_p$ we have $z' = z$ and we can extract the pump amplitudes from the integral

$$A_p(z)A_p^*(z') = |A_p(z)|^2,$$

showing that the signal dynamics is independent of the pump phase fluctuations $\Phi_p(z)$.

This means that the rapid random phase fluctuations of the pump do not affect the signal which undergoes slow phase variations and thus evolves towards a highly coherent state during its parametric amplification.

Let us now consider the idler wave from the third equation (18):

$$A_i(x, t) = \sigma \int_0^t e^{-\gamma_i(t-t')} A_p(z') A_s^*(x', t') dt'.$$

When $v_i = v_p$ we have $z' = z$ and $A_p(z')$ becomes independent of t' which leads to an idler amplitude A_i proportional to the pump amplitude A_p *i.e.*, the idler field absorbs the noise of the co-moving pump field. Note that this *pump-idler phase-locking mechanism* does not require an exact matching of the group-velocities $v_i = v_p$. It is indeed sufficient that

$$|v_i - v_p| \ll \lambda_c \gamma_i = v_p t_c \gamma_i,$$

to remove the pump field from the integral so that the idler field follows the pump fluctuations. This phase-locking mechanisms may be demonstrated in realistic experimental configurations as studied in details in Ref.[35].

6 Conclusion

We have shown by a stability analysis of the non-degenerate backward OPO where both the signal and idler fields propagate backward with respect to the direction of the pump field that the inhomogeneous stationary solutions regularly bifurcate towards a time-dependent oscillatory solution contrarily to the degenerate case. We obtain a regular Hopf bifurcation for a critical interaction length L_{crit} , which is finite only if a finite group velocity delay between the signal and the idler waves is taken into account.

This result has been confirmed by numerical simulations of the nonlinear dynamic equations, and an excellent agreement has been obtained near the degenerate configuration. Above L_{crit} self-structuration of symbiotic backward solitary waves - of some ps temporal duration - takes place. The finite temporal walk-off between the backscattered signal and idler waves also ensures the stability of the solitary waves. These short stable and coherent pulses could be very interesting for optical telecommunication. However, the susceptibility inversion grating of sub- μm period required for QPM in the nonlinear quadratic materials is still a technological challenge.

Finally we have shown that singly backward mirrorless OPO's (BMOPO's) pumped by an incoherent field are characterized, as a general rule, by the generation of a highly coherent backward field. This remarkable property finds its origin in two distinct phase-locking mechanisms. **(i)** The convection-induced phase-locking mechanism, in which the incoherence of the pump is absorbed by the co-propagating wave moving at the same group-velocity [25] [35] [36] [37]. **(ii)** The dispersion-induced phase-locking mechanism, in which the incoherence of the pump is absorbed by the co-propagating wave that exhibits the same group-velocity dispersion as the pump [38]. In both cases the incoherence of the pump is transferred to the co-moving field, which allows the backward field to evolve towards a highly coherent state. On the basis of the recent experiment reported in [24], we proposed realistic experimental conditions that may be implemented with current technology and in which backward coherent wave generation from incoherent excitation may be observed and studied. Let us finally note that it would be interesting to analyze theoretically these phenomena by making use of the kinetic wave theory [41], in line with the recent works on optical wave thermalization [42] and condensation [43].

7 Acknowledgements

The authors acknowledge the GDR PhoNoMi2 n° 3073 of the CNRS (Centre National de la Recherche Scientifique) devoted to Nonlinear Photonics in Microstructured Materials.

References

1. Armstrong J.A., Jha S.S., and Shiren N.S., IEEE J. Quant. Elect. **QE-6**, (1970) 123-129.
2. Nozaki K. and Taniuti T., J. Phys. Soc. Jpn. **34**, (1973) 796-800.
3. Kaup D.J., Reiman A., and Bers A., Rev. Mod. Phys. **51**, (1979) 275-309.
4. Driühl K., Wenzel R.G. and Carlsten J.L., Phys. Rev. Lett. **51**, (1983) 1171.
5. McCall S.L. and Hahn E.L., Phys. Rev. Lett. **18**, (1967) 908.
6. Chiu S.C., J. Math. Phys. **19** (1978) 168-176.
7. Montes C., Mikhailov A., Picozzi A., and Ginovart F., Phys. Rev. E **55**, (1997).
8. Montes C., Picozzi A., and Bahloul D., Phys. Rev. E **55**, (1997) 1092-1105.
9. Picholle E., Montes C., Leycuras C., Legrand O., and Botineau J., Phys. Rev. Lett. **66**, (1991) 1454.
10. Montes C., Mamhoud A., and Picholle E., Phys. Rev. A **49** (1994) 1344.
11. Montes C., Bahloul D., Bongrand I., Botineau J., Cheval G., Mamhoud A., Picholle E., and Picozzi A., J. Opt. Soc. Am. B **16** (1999) 932.
12. Botineau J., Cheval G., and Montes C., Opt. Commun. **257**, (2006) 319-33.
13. Montes C. *Dissipative Solitons : From Optics to Biology and Medecine* (Akhmediev, N. and Ankiewicz, A. Springer-Verlag, Berlin, 2008) 221-260.
14. Picozzi A. and Haelterman M., Opt. Lett. **23**, (1998) 1808.
15. Picozzi A. and Haelterman M., Phys. Rev. Lett. **84**, (2000) 5760-5762.
16. Montes C., Picozzi A., and Haelterman M., *Optical Solitons: Theoretical Challenges and Industrial Perspectives* (Zakharov V.E. and Wabnitz S., EDP Springer, 1999) 283-292.
17. Montes C., *Optical Solitons : Theory and Experiments* (Porsezian K. and Kuriakos V.C., Springer-Verlag, Berlin, 2003) 353-371.
18. Durniak C., Montes C. and Taki M., J.Opt. B: Quantum Semiclass. Opt. **6**, (2004) S241-S249.
19. Montes C., Durniak C., Taki M., and Picozzi A., Opt. Commun. **216**, (2003) 419-426.
20. Matsumoto M. and Tanaka K., IEEE J. Quantum Electron. **31**, (1995) 700.
21. Ding Y. J. and Khurgin J.B., IEEE J. Quantum Electron. **32**, (1996) 1574-1582.
22. Kang J.U., Ding Y.J., Burns W.K., and Melinger J.S., Opt. Lett. **22**, (1997) 862.
23. D'Alessandro G., Russell P.St., and Wheeler A.A., Phys. Rev. A **55**, (1997) 3211.
24. Canalias C. and Pasiskevicius V., Nature Photonics, **1**, (2007) 459-462.
25. Picozzi A. and M. Haelterman M., Phys. Rev. Lett., **86**, (2001) 2010.
26. Morozov S.F., Piskunova L.V., Sushchik M.M., and Freidman G.I., Sov. J. Quant. Electron. **8**, (1978) 576.
27. Craik A.D.D., Nagata M., and Moroz I.M., Wave Motion **15**, (1992) 173.
28. Armstrong J.A., Bloembergen N., Ducuing J. and Pershan N. Phys. Rev. **127** (1962) 1918-1939.
29. Busacca A.C., Sones C.L., Eason R.W., and Mailis S., Applied Phys. Lett. **84**, (2004) 4430-4432.
30. Dmitriev V.G., Gurzadyan G.G., Nikogosyan D.N., *Handbook of Nonlinear Optical Crystals* (Springer-Verlag, Berlin, 1991) 74 for LiNbO₃ and 103 for KTiOPO₄.
31. Bava G.P., Montrosset I., Sohler W., and Suche H., IEEE J. Quantum Electron. **QE-23**, (1987) 42.
32. Suche H. and Sohler W., *Integrated optical parametric oscillators* (invited), Optoelectronics-Devices and Technologies, Japan, **4**(1), (1989) 1-20.
33. Arbore M.A. and Fejer M.M., Opt. Lett. **22**, (1997) 151-153.
34. Hofmann D., Herrmann H., Schreiber G., Grundkötter W., Ricken R., and Sohler W., *Continuous-wave mid-infrared optical parametric oscillators with periodically poled Ti:LiNbO₃ waveguide*, in *9th European Conference on Integrated Optics and Technical Exhibition ECIO'99* (EOS - European Optical Society 1999), p. 21; Hofmann D., Herrmann H., Schreiber G., Haase C., Grundkötter W., Ricken R., and Sohler W., in *Nonlinear Guided Waves and Their Applications* (Optical Society of America, Washington, D.C., 1999), FC2-1-3, p.465.
35. Picozzi A., Montes C., and Haelterman M., Phys. Rev E **66**, (2002) 056605-1-14.
36. Montes C., Picozzi A., and Gallo K., Opt. Commun. **237**, (2004) 437-449.
37. Montes C., Grundkötter W., Suche H., and Sohler W., J. Opt. Soc. Am. **24** (2007) 112796-11280.
38. Picozzi A. and Aschieri P., Phys. Rev. E **72**, (2005) 046606-1-12.
39. Harris S.E. Appl. Phys. Lett. **9** (1966) 114
40. Shi W. and Ding Y.J., Optics Lett. **30** (2005) 1861-1863.
41. Zakharov V.E., L'vov V.S. and Falkovich G., *Kolmogorov Spectra of Turbulence I* (Springer, Berlin, 1992); Newell A.C., Nazarenko S. and Biven L., Physica D **152-153**, (2001) 520-550; Zakharov V., Dias F. and Pushkarev A., Phys. Rep. **398**, (2004) 1.

42. Pitois S., Lagrange S., Jauslin H. R., and Picozzi A., Phys. Rev. Lett. **97**, (2006) 033902; Lagrange S., Jauslin H.R. and Picozzi A., Europhys. Lett. **79**, (2007) 64001; Picozzi A., Opt. Express **16**, (2008) 17171; Barviau B., Kibler B., Coen S. and Picozzi A., Opt. Lett. **33**, (2008) 2833; Picozzi A., Pitois S. and Millot G., Phys. Rev. Lett. **101**, (2008) 093901.
43. Dyachenko S., Newell A. C., Pushkarev A., and Zakharov V.E., Physica D **57**, (1992) 96; Connaughton C., Josserand C., Picozzi A., Pomeau Y., and Rica S., Phys. Rev. Lett. **95**, (2005) 263901; Zakharov V.E. and Nazarenko S.V., Physica D **201**, (2005) 203; Picozzi A., Opt. Express **15**, (2007) 9063; Picozzi A. and Rica S., Europhys. Lett. **84**, (2008) 34004.

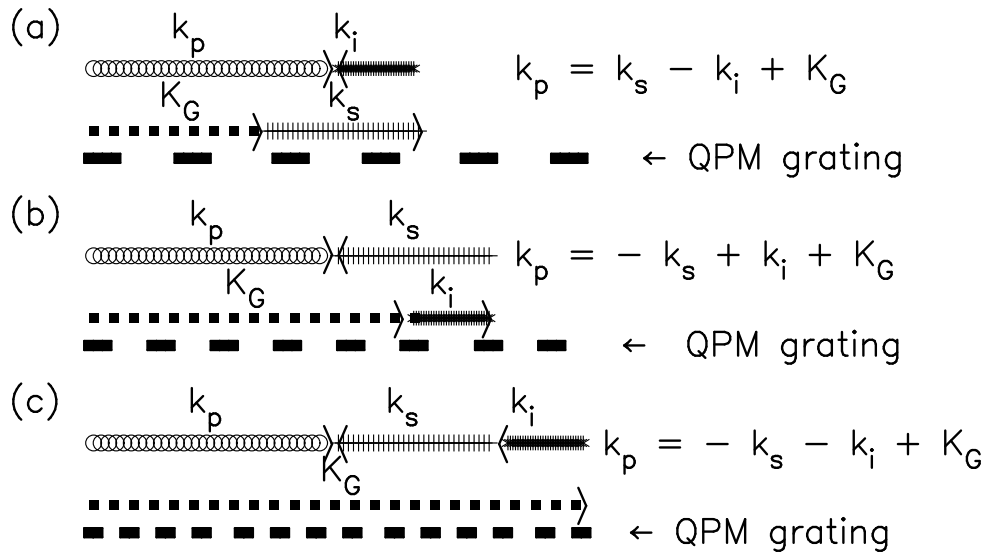


Fig. 1. Wave vector diagrams (momentum conservation) for the non-degenerate three-wave interaction in: a singly backward idler configuration (a); a singly backward signal configuration (b); and a doubly backward (signal and idler) configuration (c). As we can see the QPM grating show a decreasing phase-reversal period for the nonlinear susceptibility represented by the bold broken lines under each configuration.

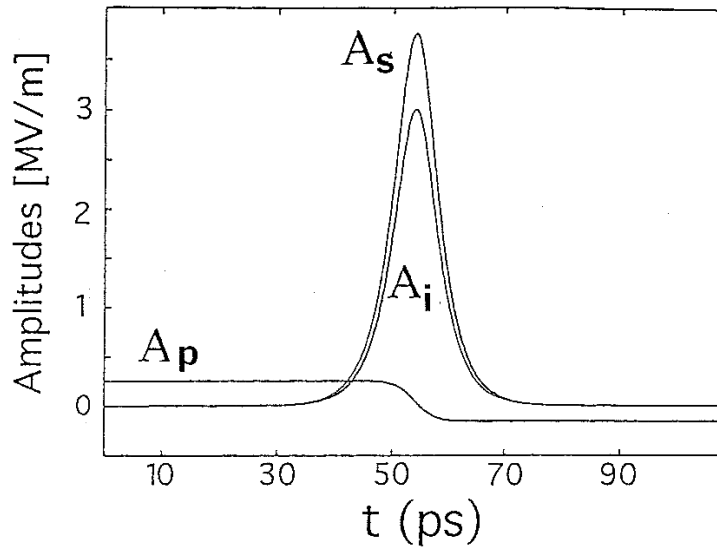


Fig. 2. Envelopes of the dissipative three-wave solitary solution.

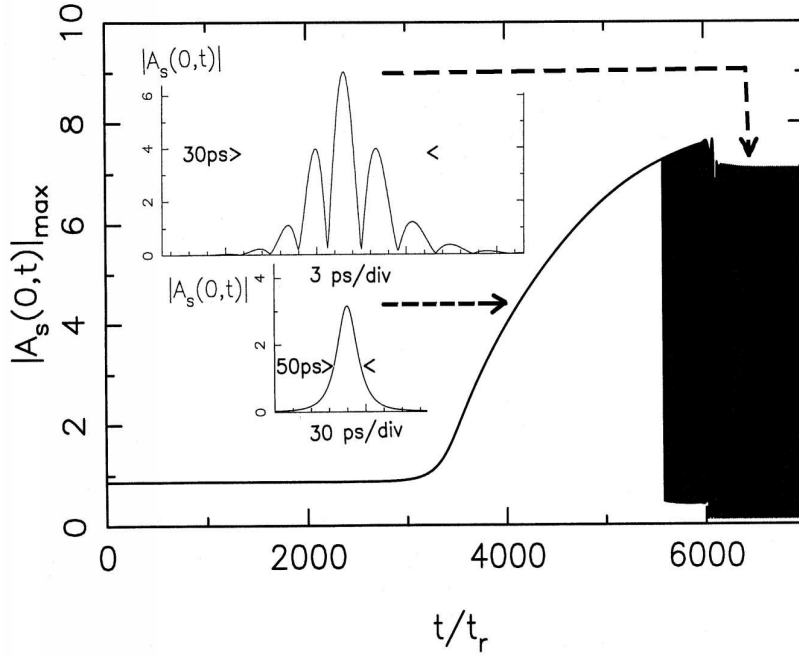


Fig. 3. Degenerate backward OPO: Pulse maximum amplitude *vs.* number of round trips t/t_r (where $t_r = \ell/v_s$ is the round-trip time) at the output of the backward OPO cavity exhibiting the unstable temporal process; numerical solution of the degenerate equations derived from equations (1) by starting from the inhomogeneous steady solution. The lower inset graph shows the generated pulse structure before saturation, which takes place about 6000 round trips, when the pulse is so steep that dispersion breaks the unlimited amplification by modulating the pulse. The upper inset graph shows the time-dependent modulated structure. Dimensionless parameters are: $L = \ell/\Lambda = 1$; $\rho_s = \sqrt{R} = 0.46$; $\beta_s/\tau_0 = 5 \times 10^{-6}$.

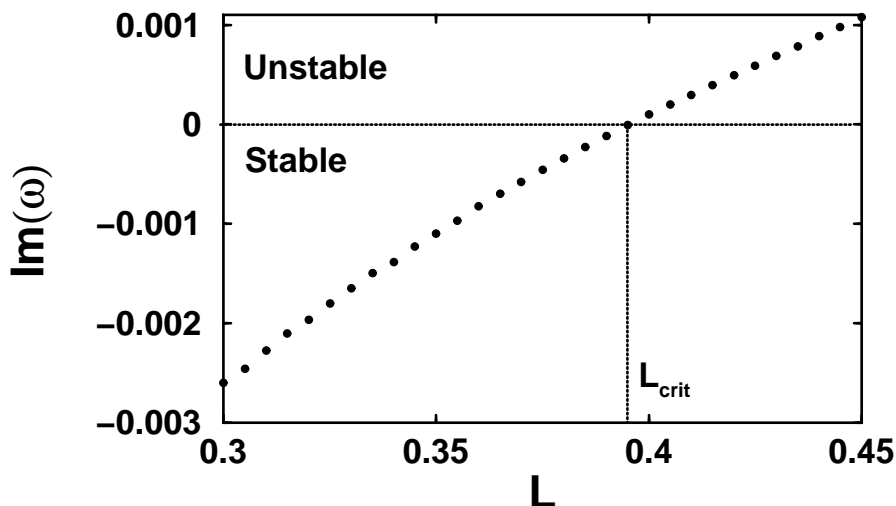


Fig. 4. Evolution of the imaginary part of the pulsation ω as a function of the length L close to the first cavity mode (with $\text{Re}(\omega) \simeq 2\pi/L$). The transition from stable to unstable states is obtained for $L_{\text{crit}} \simeq 0.39$.

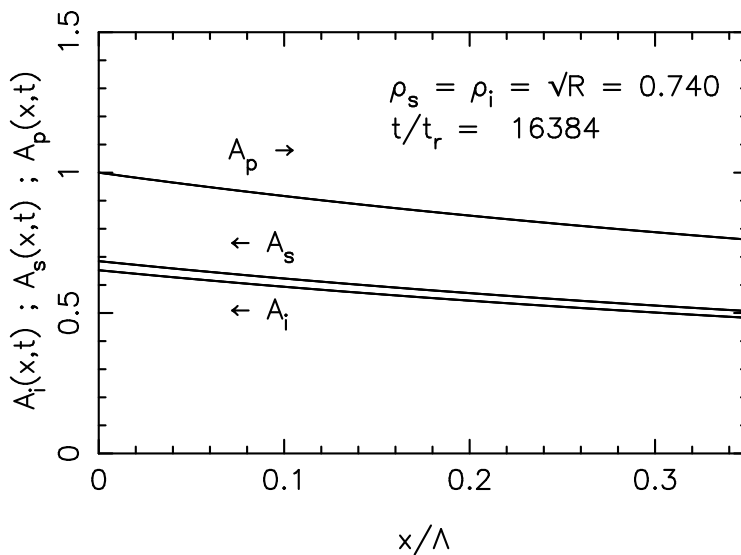


Fig. 5. Doubly resonant backward OPO: asymptotic stationary spatial profiles at round trip 16384 for $L = 0.35$ below critical length.

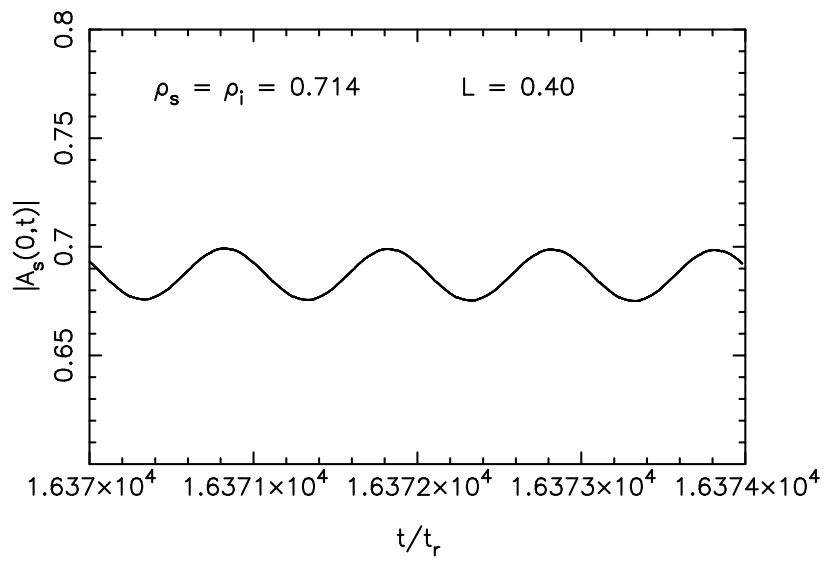


Fig. 6. Doubly resonant backward OPO: temporal oscillatory regime for $L = 0.4$ above critical length.

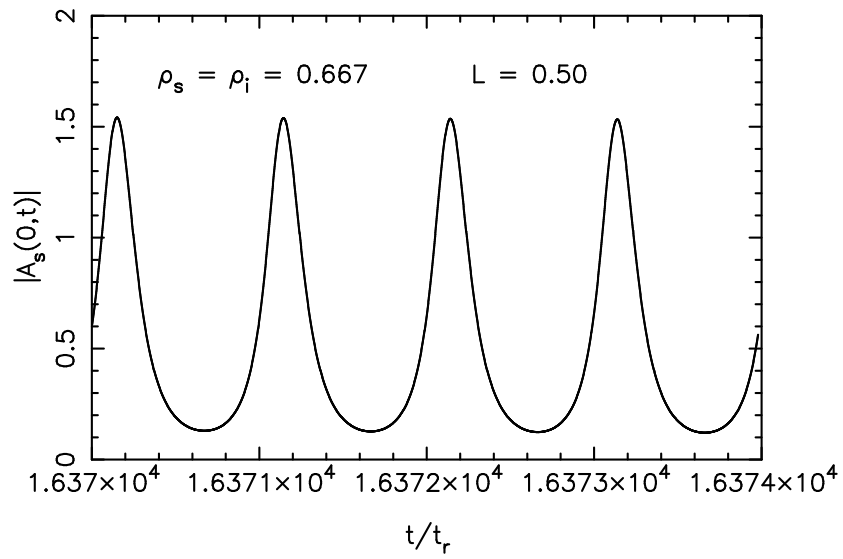


Fig. 7. Doubly resonant backward OPO: temporal pulsed regime for a length $L = 0.5$.

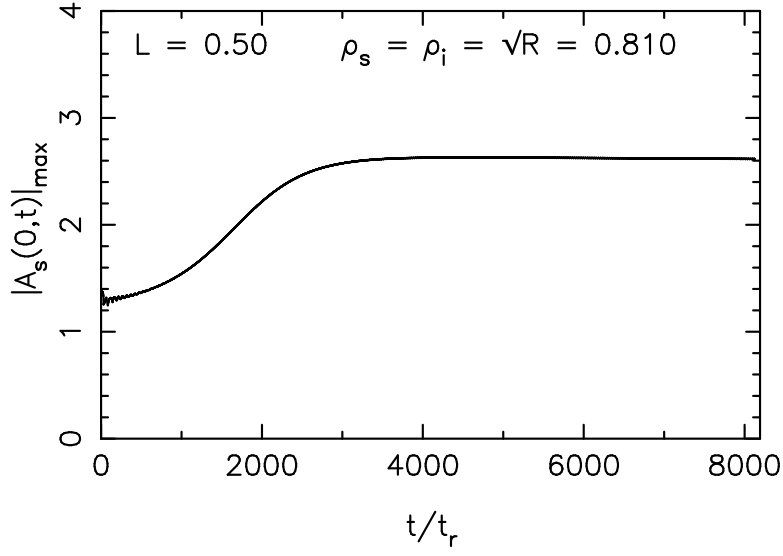


Fig. 8. Doubly resonant backward OPO: pulse maximum amplitude *vs.* number of round trips t/t_r (where $t_r = \ell/v_s$ is the round-trip time) at the output of the backward OPO cavity exhibiting stable saturation at a constant amplitude.

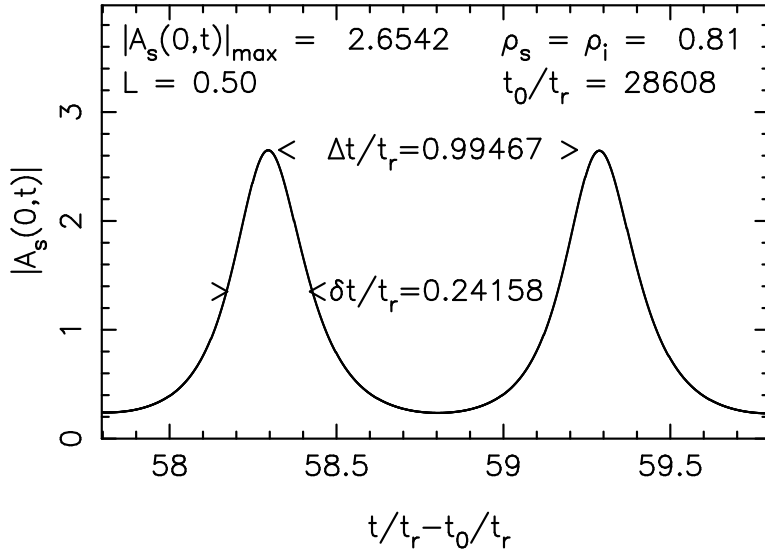


Fig. 9. Doubly resonant backward OPO: temporal evolution of a pulse train at the output of the OPO cavity. Pair of two consecutive pulses at round trip $t/t_r = 28608$ for $L = 0.5$ and $\rho_s = \rho_i = 0.81$. The amplitude is measured in $|A_{p,o}|/\sqrt{2}$ units.

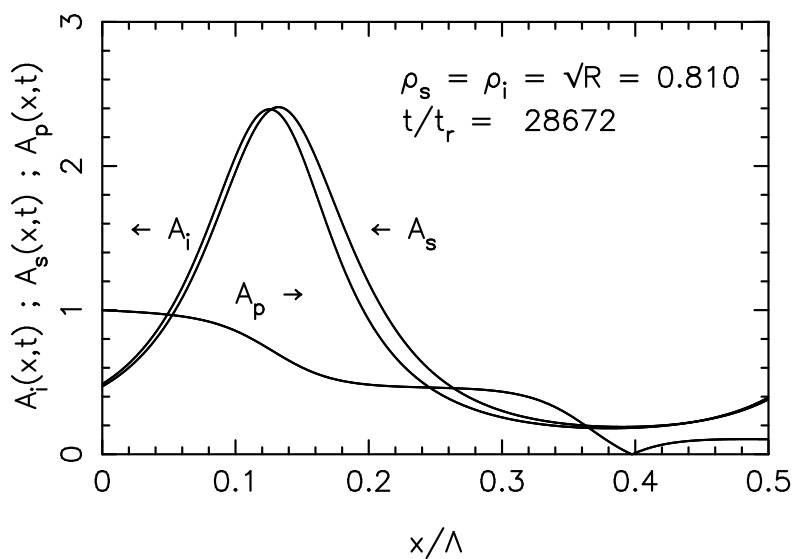


Fig. 10. Doubly resonant backward OPO: spatial profiles for the three wave amplitudes at round trip 28672.

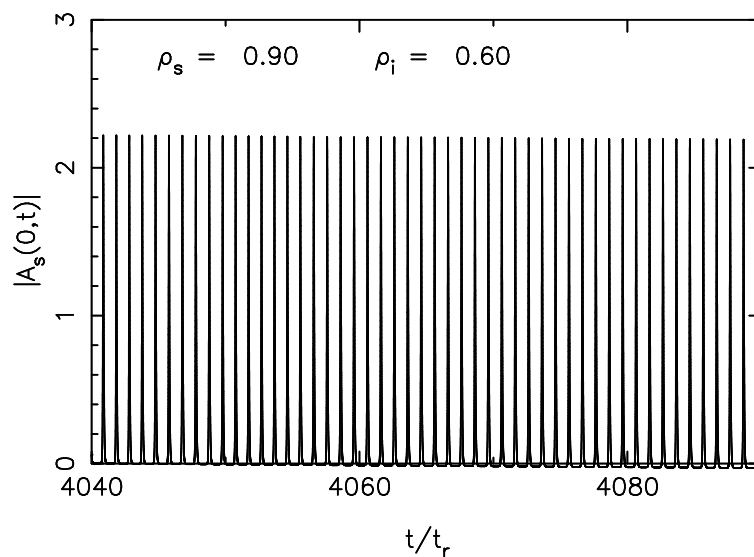


Fig. 11. Doubly resonant backward OPO: temporal amplitude signal output of the backward OPO in the stable asymptotic pulsed regime measured in cavity round trips t/t_r for $L = 1$, $\rho_s = 0.90$, $\rho_i = 0.60$ and $\tilde{\beta}_j = 10^{-6}$, $j = p, s, i$.

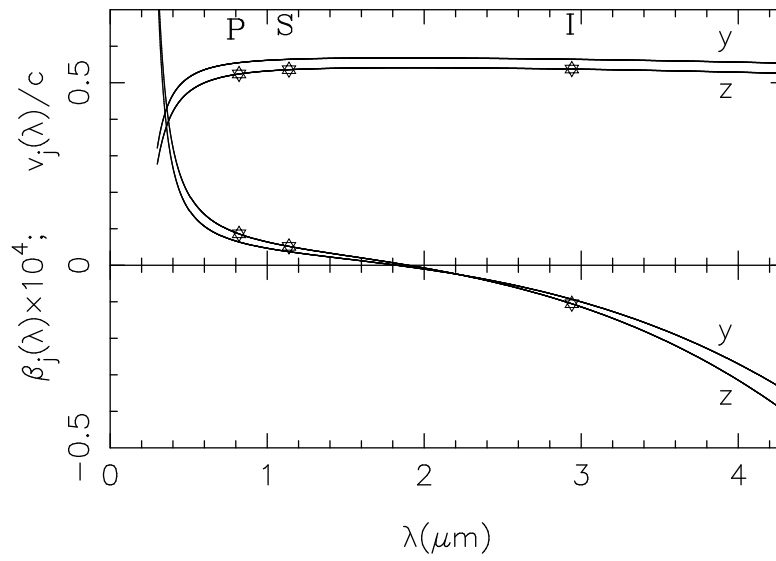


Fig. 12. BMOPO I: Group-velocity dispersion for KTiOPO_4 at 20°C . Experimental achieved point of operation for the type I configuration [24].

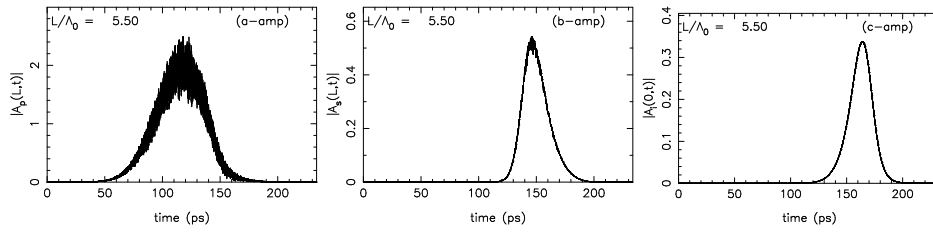


Fig. 13. BMOPO I: Temporal field amplitude output of pump (a), signal (b) and counterpropagating idler (c) waves in the achieved experimental configuration [24], for a pump of ns temporal duration and 220 GHz incoherent bandwidth.

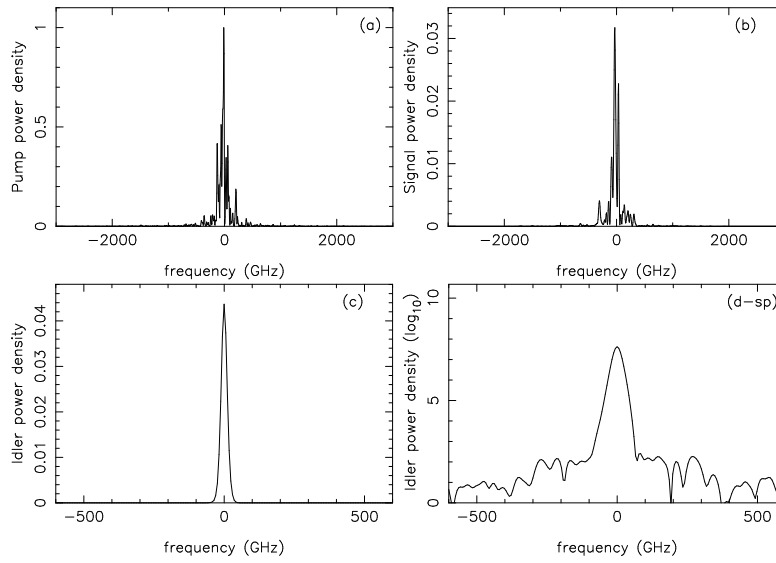


Fig. 14. BMOPO I: Respective power spectra of pump (a), signal (b) and counterpropagating idler (c) [(d) in log scale] for the incoherent pump of 220 GHz bandwidth, showing a coherence transfer rate $\Delta\nu_i/\Delta\nu_p \simeq 1/30$.

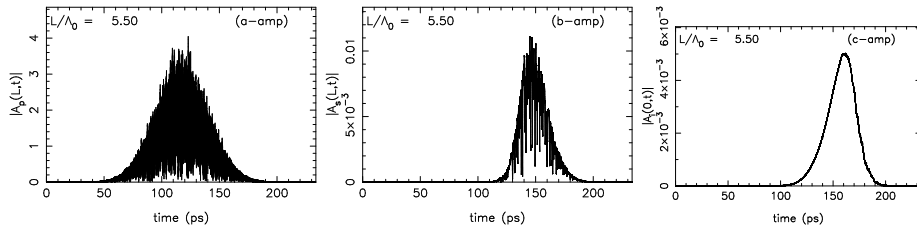


Fig. 15. BMOPO I: Temporal field amplitude output of pump, signal and counterpropagating idler waves in the achieved experimental configuration [24], for an incoherent pump of 1500 GHz bandwidth.

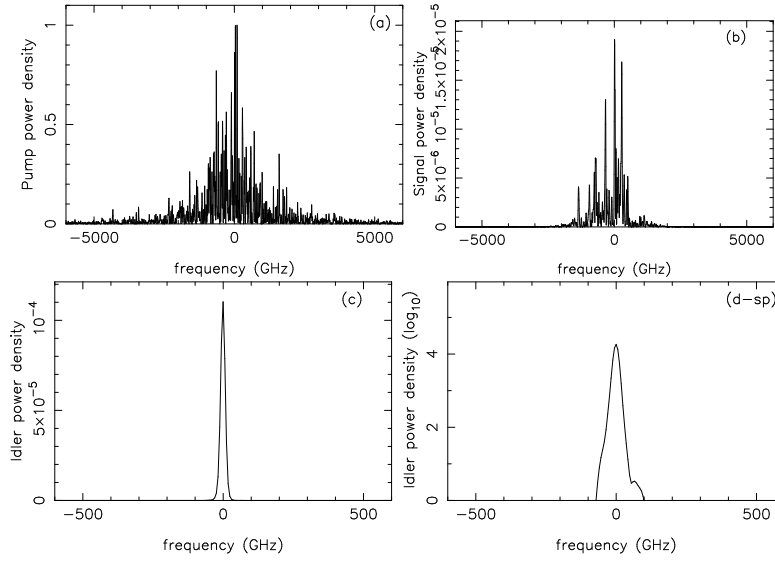


Fig. 16. BMOPO I: Respective power spectra of pump (a), signal (b) and counterpropagating idler (c) [(d) in log scale] for the incoherent pump of 1500 GHz bandwidth, showing a coherence transfer rate $\Delta\nu_i/\Delta\nu_p \simeq 1/600$.

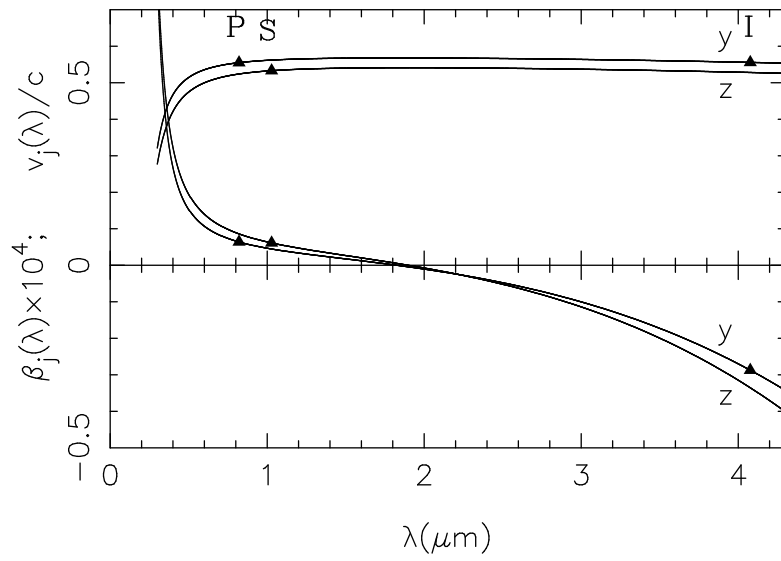


Fig. 17. BMOPO II: Group-velocity dispersion for KTiOPO_4 at 20°C . Point of operation for dispersion mismatch between pump and signal ($\beta_p = \beta_s$) as show the underneath curves.

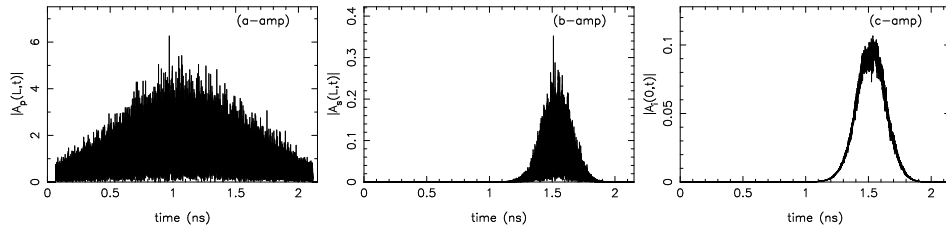


Fig. 18. BMOPO II: Temporal field amplitude output of pump (a), signal (b) and counterpropagating idler (c) waves in the BMOPO II, for an incoherent pump of 25 THz bandwidth.

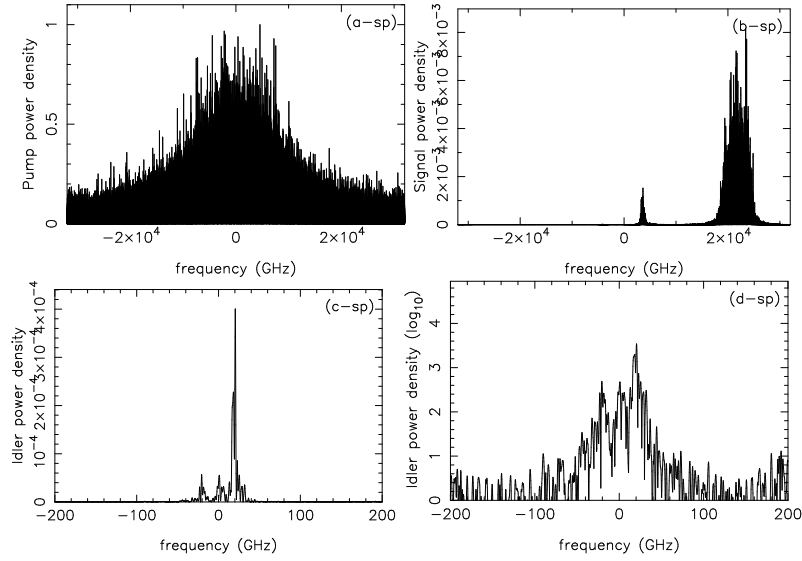


Fig. 19. BMOPO II: Respective power spectra of pump (a), signal (b) and counterpropagating idler (c) [(d) in log scale] for the incoherent pump of 25 THz bandwidth, showing a coherence transfer $\Delta\nu_i/\Delta\nu_p \simeq 1/2000$.

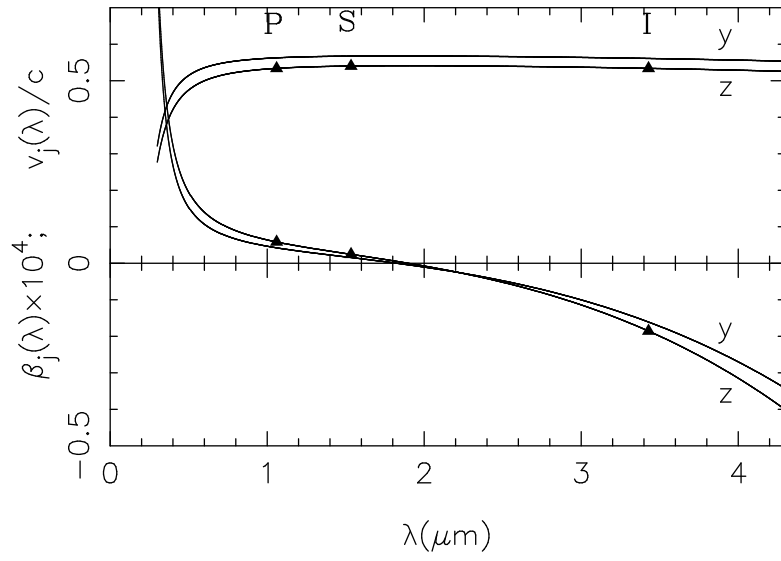


Fig. 20. BMOPO III: Group-velocity dispersion for KTiOPO_4 at 20°C . Point of operation for group velocity mismatch ($v_p = v_i$) between pump and idler shown in the upper curves.

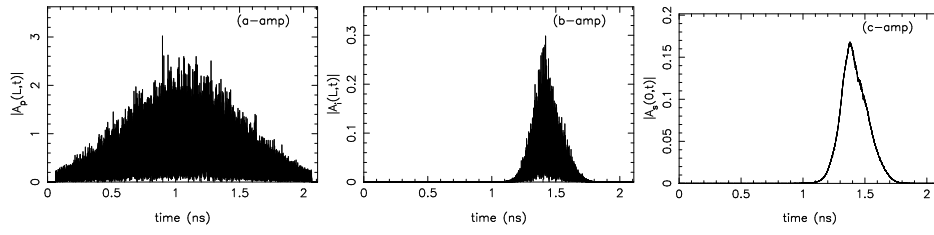


Fig. 21. BMOPO III: Temporal field amplitude output of pump (a), idler (b) and counterpropagating signal (c) waves in the BMOPO III, for an incoherent pump of 25 THz bandwidth.

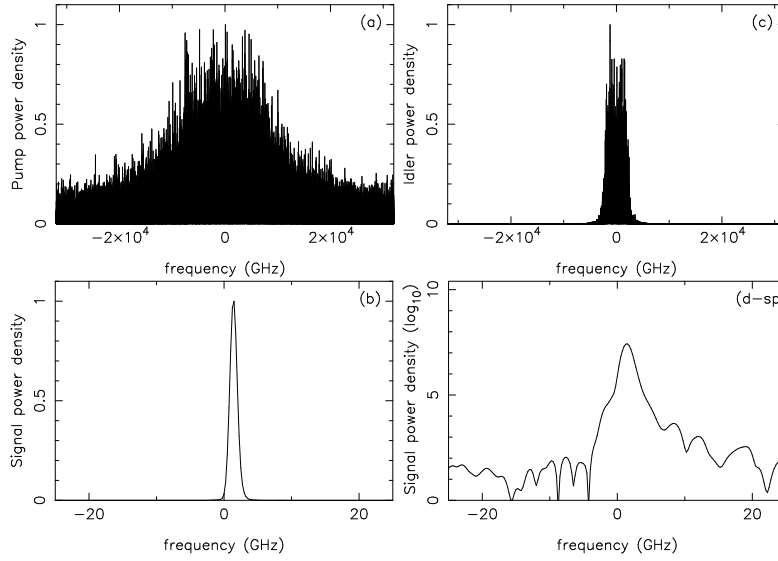


Fig. 22. BMOPO III: Respective power spectra of pump (a), idler (b) and counterpropagating signal (c) [(d) in log scale] for the incoherent pump of 25 THz bandwidth, showing a high coherence transfer rate $\Delta\nu_s/\Delta\nu_p \simeq 1/8000$.